

Comparative study on electronic structures of two phases compounds and origin of the structural phase transition in $LiFePO_4$

Peiru Yang(杨佩如), Xinchun Du(杜新春), Jie Li(李杰), Siqi Shi(施思齐)

Citation: Chin. Phys. B, 2025, 34 (**11**): 118201. DOI: 10.1088/1674-1056/ae0bfe
http://cpb.iphy.ac.cn; http://iopscience.iop.org/cpb

What follows is a list of articles you may be interested in

Influence of carbon sources on the performance of carbon-coated nano-silicon

Lin Wang(王琳), Na Li(李娜), Hao-Sen Chen(陈浩森), and Wei-Li Song(宋维力)
Chin. Phys. B, 2023, 32 (**10**): 108201. DOI: 10.1088/1674-1056/acb9e9

Stress effect on lattice thermal conductivity of anode material $NiNb_2O_6$ for lithium-ion batteries

Ao Chen(陈奥), Hua Tong(童话), Cheng-Wei Wu(吴成伟), Guofeng Xie(谢国锋), Zhong-Xiang Xie(谢忠祥), Chang-Qing Xiang(向长青), and Wu-Xing Zhou(周五星)
Chin. Phys. B, 2023, 32 (**5**): 058201. DOI: 10.1088/1674-1056/acaa2d

In situ formed FeS_2@CoS cathode for long cycling life lithium-ion battery

Xin Wang(王鑫), Bojun Wang(汪博筠), Jiachao Yang(杨家超), Qiwen Ran(冉淇文), Jian Zou(邹剑), Pengyu Chen(陈鹏宇), Li Li(李莉), Liping Wang(王丽平), and Xiaobin Niu(牛晓滨)
Chin. Phys. B, 2021, 30 (**8**): 088201. DOI: 10.1088/1674-1056/abe9ab

Neutron-based characterization techniques for lithium-ion battery research

Enyue Zhao(赵恩岳), Zhi-Gang Zhang(张志刚), Xiyang Li(李西阳), Lunhua He(何伦华), Xiqian Yu(禹习谦), Hong Li(李泓), Fangwei Wang(王芳卫)
Chin. Phys. B, 2020, 29 (**1**): 018201. DOI: 10.1088/1674-1056/ab5d07

Influence of carbon coating on the electrochemical performance of SiO@C/graphite composite anode materials

Hao Lu(陆浩), Junyang Wang(汪君洋), Bonan Liu(刘柏男), Geng Chu(褚赓), Ge Zhou(周格), Fei Luo(罗飞), Jieyun Zheng(郑杰允), Xiqian Yu(禹习谦), Hong Li(李泓)
Chin. Phys. B, 2019, 28 (**6**): 068201. DOI: 10.1088/1674-1056/28/6/068201

SPECIAL TOPIC — Structures and properties of materials under high pressure

Comparative study on electronic structures of two phases compounds and origin of the structural phase transition in $LiFePO_4$

Peiru Yang(杨佩如), Xinchun Du(杜新春), Jie Li(李杰)[†], and Siqi Shi(施思齐)[‡]

School of Materials Science and Engineering, Shanghai University, Shanghai 200444, *China*

(Received 16 July 2025; revised manuscript received 15 September 2025; accepted manuscript online 26 September 2025)

$LiFePO_4$ has normal olivine-structured (α-LFP) and high pressure (β-LFP) phases, with the former being one of the cathode materials for commercial Li-ion batteries. Despite extensive focus on the respective electrochemical properties of the two phases, there is a lack of comparative studies on their electronic and magnetic properties, and the origin of the structural phase transition remains unclear. By combining first-principles calculations with molecular dynamics simulations, we find that the anisotropic compression of Li–O bonds drives the structural phase transition from α-LFP to β-LFP at a critical pressure of 20 GPa, while β-LFP undergoes a transition from semiconductor to metal due to Fe^{3+} generated during delithiation. Their antiferromagnetic (AFM) ground states are predicted to arise from the negative magnetic exchange interactions between nearest and next-nearest neighbor sites, with the corresponding Néel temperature showing significant enhancement under pressure. Furthermore, compared with α-LFP, β-LFP shows increases in bulk, shear, and Young's moduli of 8%, 13%, and 12%, respectively. These findings enrich the physical property data of $LiFePO_4$ phase compounds, providing knowledge for expanding the application scenarios of the α-LFP phase under special operating conditions such as high pressure.

Keywords: lithium-ion battery, $LiFePO_4$, structural phase transition, first-principles calculations

PACS: 82.47.Aa, 63.20.dk

DOI: 10.1088/1674-1056/ae0bfe **CSTR:** 32038.14.CPB.ae0bfe

1. Introduction

Olivine-structured $LiFePO_4$ (LFP), as one of the most successful cathode materials in commercialized batteries, has garnered significant research attention in recent decades[1–4] owing to its reversible Li^+ intercalation/deintercalation, long cycle life, low cost, and environmental friendliness.[5,6] To date, many methods have been proposed and applied to optimize LFP cathode material, including micronization,[7,8] ligand-chain modification,[9] prelithiation,[10] and doping.[11–14] However, the low electronic conductivity and moderate energy density of LFP limit its performance in fast charging and discharging of lithium-ion batteries.[15,16] Thus, exploring the multi-physics coupling among electrons, ions, magnetism, pressure, defects, and temperature is highly necessary for optimizing LFP cathode material.[17–20]

Among various factors influencing the performance of LFP, pressure plays one of the most critical and complex roles. It is established that LFP undergoes a structural phase transition from α-LFP to β-phase (β-LFP) under high pressure, primarily driven by Li^+ migration. For instance, this transition was first reported to occur at 6.5 GPa by García-Moreno *et al.*[21] and also observed at 3.3 GPa by Lin *et al.*,[22] while Dong *et al.*[23] noted only anisotropic lattice compression without a clear phase transition up to 28.2 GPa. Meanwhile, phase transitions have also been shown to significantly influence Li^+ migration behavior, which may open up new possibilities for the development of LFP with higher packing density and volumetric energy density.[24,25] However, a consensus on the critical pressure and the origin of the phase transition has not yet been established. In addition to the structural phase transition, a pressure-induced magnetic phase transition from antiferromagnetic to non-magnetic state has also been reported.[21] Therefore, it is essential to systematically investigate both structural and magnetic phase transitions, along with their impacts on the electrochemical performance of LFP, facilitating its development as a high-performance cathode material.[22]

In this work, we systematically investigate the structural, electronic, and magnetic properties of LFP in two different phases. By using first-principles calculations combined with molecular dynamics (MD) simulations, we identify that the critical pressure for the phase transition is 20 GPa, and the anisotropic compression of Li–O bonds is the most significant factor in the structural phase transition process. Additionally, our results show that β-LFP exhibits higher electronic conductivity and enhanced mechanical properties compared to α-LFP, indicating that a cathode material comprising

[†]Corresponding author. E-mail: lij@shu.edu.cn

[‡]Corresponding author. E-mail: sqshi@shu.edu.cn

© 2025 Chinese Physical Society and IOP Publishing Ltd. All rights, including for text and data mining, AI training, and similar technologies, are reserved.

both α-LFP and a moderate amount of β-LFP is expected to be a promising candidate for high-performance electrodes for lithium-ion batteries.

2. Methods

All first-principles calculations are performed using density functional theory (DFT) with the Perdew–Burke–Ernzerhof (GGA-PBE) generalized gradient approximation, as implemented in the Vienna *Ab initio* Simulation Package (VASP).[26,27] A Hubbard U value of 4.3 eV is adopted to describe the electron correlation in the d orbitals of Fe.[28] In our calculations, the cutoff energy for wave functions is set to 500 eV, and geometric optimization is performed using the conjugate gradient method until the forces on each atom are below 0.01 eV/Å, with a total energy convergence criterion of 10^{-5} eV. Li^+ migration barriers are calculated using the climbing image nudged elastic band (CINEB) method.[29] The *ab initio* molecular dynamics (AIMD) simulations are performed using the NPT ensemble (isothermal-isobaric ensemble) with the Parinello–Rahman algorithm.[30] The Langevin thermostat is employed, with appropriate adjustments applied during the NPT simulations.

3. Results and discussion

As shown in Fig. 1(a), α-LFP adopts an olivine structure composed of FeO_6 octahedra and PO_4 tetrahedra. Li ions occupy channels along the [010] direction and form LiO_6 octahedra with the surrounding O atoms, forming a one-dimensional pathway that facilitates rapid Li^+ insertion and extraction. In contrast, in β-LFP, FeO_6 octahedra are linked to LiO_4 and PO_4 tetrahedra through corner-sharing. Based on our DFT calculation results, the lattice parameters of α-LFP (β-LFP) are $a = 4.75$ Å, $b = 6.06$ Å, $c = 10.42$ Å ($a = 5.63$ Å, $b = 6.20$ Å, $c = 8.34$ Å), respectively, which agree well with previous work.[31–34] Meanwhile, compared to β-LFP, α-LFP has an energy advantage of 0.12 eV/f.u. Extended calculations show that the energy advantage of α-LFP gradually decreases as the hydrostatic pressure increases, eventually becoming the β-LFP ground state, consistent with previous work[22] (see the inset of Fig. 1(b)). The critical pressure for the phase transition is approximately 20 GPa. Additionally, the [001] direction of α-LFP is the most sensitive to compression under hydrostatic pressure (nearly 6.4% under 20 GPa). During this process, the volumes of the LiO_6, FeO_6, and PO_4 polyhedra decrease by 16.5%, 11.3%, and 4.5%, respectively (as shown in the top inset of Fig. 1(b)). Their corresponding mechanical characteristics are further explored and shown in Table S1. The calculated bulk modulus of α-LFP is 93.6 GPa, which agrees well with the experimental result,[23] whereas β-LFP exhibits a higher bulk modulus of 101.5 GPa. Moreover, β-LFP also shows larger shear and Young's moduli compared to α-LFP (see Table S1), indicating that β-LFP has stronger mechanical properties.

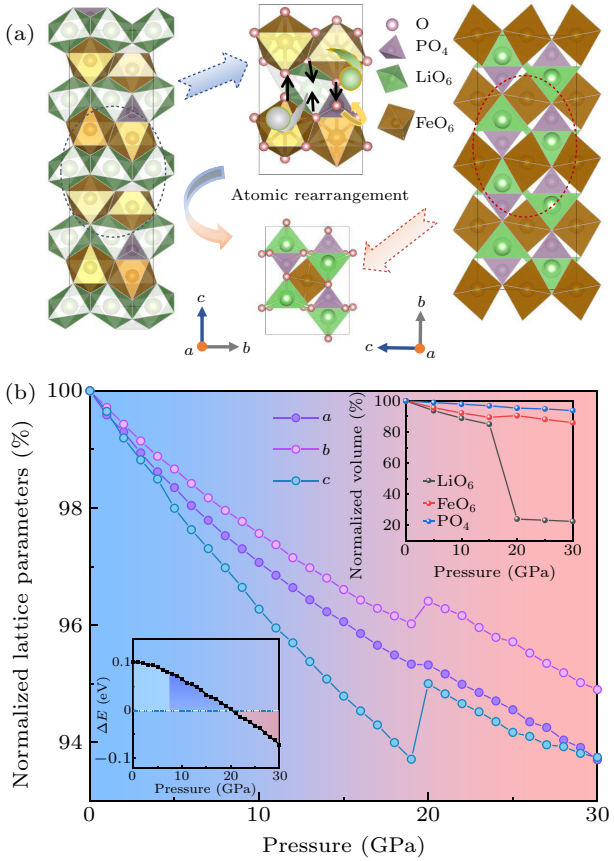


Fig. 1. (a) Schematic illustration of the structural phase transition of LFP from α-LFP to β-LFP. (b) The lattice constants as a function of pressure. The bottom inset shows the total energy difference as a function of pressure ($\Delta E = E_{\beta-\mathrm{LFP}} - E_{\alpha-\mathrm{LFP}}$, where $E_{\alpha-\mathrm{LFP}}$ and $E_{\beta-\mathrm{LFP}}$ denote the total energies of α-LFP and β-LFP, respectively). The top inset shows the relative volumes of LiO_6, FeO_6, and PO_4 polyhedra as a function of pressure.

To obtain a clear picture of the structural phase transition, AIMD simulations starting from relaxed α-LFP with a $2 \times 2 \times 1$ supercell (112 atoms) are performed at 300 K and 30 GPa for 20 ps (10000 steps) using the NPT (isothermal-isobaric) ensemble. As shown in Figs. 2(a) and 2(c), each Li atom in α-LFP is coordinated by six nearest and two next-nearest oxygen atoms, with Li–O bond lengths of 2.00 Å and 3.38 Å, whereas β-LFP has four nearest and four next-nearest oxygen atoms, with shorter nearest (1.92 Å) and next-nearest (3.00 Å) Li–O bond lengths.

Under pressure, the lattice parameters further decrease as the AIMD simulations proceed (see Fig. S3), with the [001] direction exhibiting greater sensitivity than other directions due to the weaker interplane Li–O–Fe bonding compared to intraplane Li–O–Li bonding. This anisotropy causes the Li atoms to move away from the center of the LiO_6 octahedron, forming LiO_4 tetrahedra with four nearest oxygen atoms, signifying the

occurrence of the phase transition from α-LFP to β-LFP. As shown in Figs. 2(c) and 2(d), the number of nearest oxygen atoms around each Li atom decreases, whereas the number of next-nearest oxygen atoms increases as the AIMD simulations proceed. Thus, the phase transition from α-LFP to β-LFP can be expected, even though the clear phase transition process was not directly observed in the relatively short AIMD simulations (20 ps). Meanwhile, AIMD simulation results under lower pressures (1 GPa and 6 GPa) further show that the fraction of local β-LFP decreases as the pressure decreases (see Fig. S5), suggesting that pressure provides a possible means to introduce local β-LFP for further modification of α-LFP.

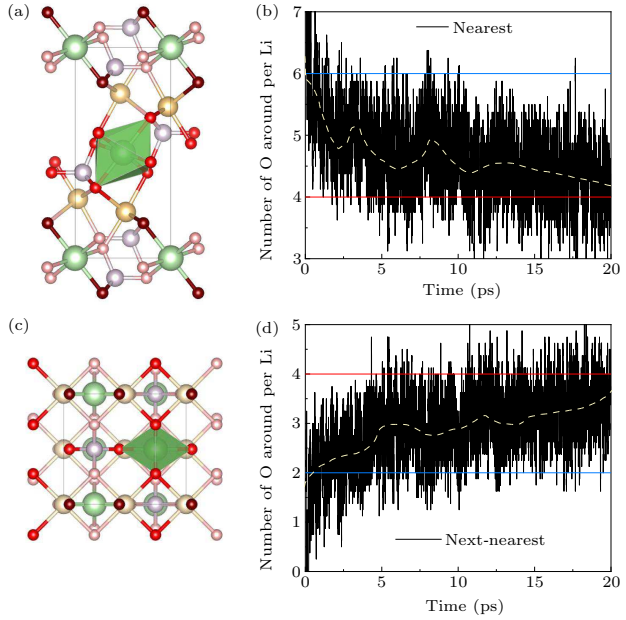


Fig. 2. (a) and (c) Schematic structures of the nearest (red) and next-nearest (wine red) O atoms around a Li atom for α-LFP and β-LFP, respectively. (b) and (d) The average numbers of nearest and next-nearest O atoms around a Li atom as a function of AIMD simulation time.

For LFP, one of the most successful commercialized cathode materials, the Li^+ migration barrier is a critical parameter governing its electrochemical performance. The potential Li^+ migration pathways in both phases are depicted in Figs. 3(a) and 3(b). DFT calculations reveal that the Li^+ migration barriers along the *b*-axis (path 1), *a*-axis (path 2), and *ac*-plane (path 3) in α-LFP are 0.49 eV, 2.1 eV, and 2.3 eV, respectively, indicating that α-LFP possesses a one-dimensional channel along the *b*-axis that facilitates rapid Li^+ insertion and extraction. In contrast, β-LFP exhibits two distinct Li^+ migration pathways, where Path 1 shows a lower energy barrier (1.39 eV) than Path 2 (1.52 eV). The significantly higher migration barriers in β-LFP are attributed to its lower coordination number compared to α-LFP. In α-LFP, Li forms LiO_6 octahedra with six surrounding oxygen atoms, whereas in β-LFP, each Li^+ ion is coordinated to only four oxygen atoms, forming a more compact tetrahedral LiO_4 unit. The adjacent LiO_4, FeO_6, and PO_4 polyhedra share a common vertex, significantly reducing the available space for Li^+ migration and further restricting diffusion pathways. Additionally, adjacent Li^+ sites, surrounded by octahedral FeO_6 and tetrahedral PO_4 units, reduce the available migration cavities and lead to more tortuous diffusion pathways. Hence, Li^+ migration in β-LFP requires more energy to overcome the barriers between neighboring Li^+ sites. Our DFT results demonstrate that the poor Li^+ mobility in β-LFP leads to inferior electrochemical performance, in agreement with previous studies.[35]

Furthermore, DFT calculations show that the magnetic configuration of LFP has a significant impact on the Li^+ migration barrier. When magnetism is not included, the barrier is only 0.33 eV for α-LFP, which agrees well with previous computational work,[23] but it is still underestimated compared to experimental measurements.[36,37] After including magnetic effects, the DFT results agree well with these experimental measurements, and the barrier increases to 0.49 eV (see Fig. S8). Therefore, we will further explore the magnetic properties of LFP in the next section. In addition to magnetic interactions, the effect of pressure on Li^+ migration cannot be neglected, as our calculations reveal that the Li^+ migration barriers of both α-LFP and β-LFP gradually increase under pressure (see Fig. S9).

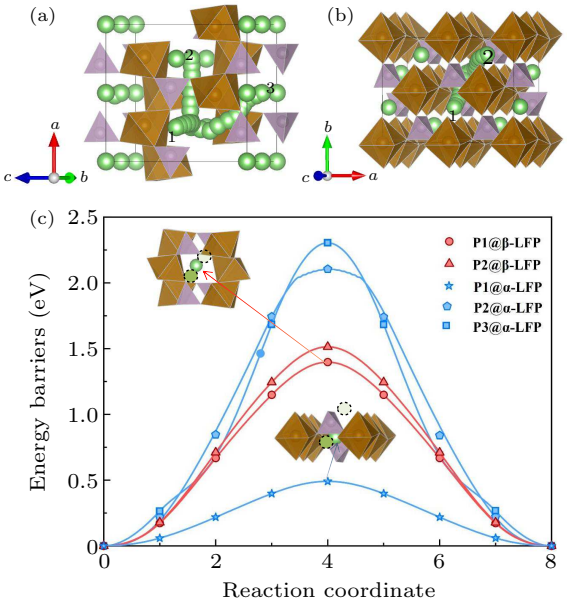


Fig. 3. (a) and (b) Schematic Li^+ diffusion paths for α-LFP and β-LFP, respectively. (c) Energy profiles of Li^+ in α-LFP and β-LFP.

To explore the magnetic properties of LFP, an effective Heisenberg spin Hamiltonian was constructed as

$$H = -J_1\sum_{i,j}(S_iS_j) - J_2\sum_{i,j}(S_iS_j) - J_3\sum_{i,j}(S_iS_j) - J_4\sum_{i,j}(S_iS_j), \quad (1)$$

where J_1 and J_2 are the nearest and next-nearest neighbor exchange interaction parameters for in-plane superexchange coupling, while J_3 and J_4 are the exchange interaction parameters for interplane superexchange coupling (as shown in Fig. S10). $S_{i,j}$ denotes the spin quantum number of a Fe atom ($S = 2$). Based on Eq. (1), the total energies of five spin configurations, as shown in Figs. S11 and S12, can be expressed as

$$E_{\mathrm{FM}} = (-2J_1 - J_2 - J_3 - J_4)S^2 + E_0,$$
$$E_{\mathrm{AFM1}} = (2J_1 - J_2 + J_3 - J_4)S^2 + E_0,$$
$$E_{\mathrm{AFM2}} = (2J_1 - J_2 - J_3 + J_4)S^2 + E_0,$$
$$E_{\mathrm{AFM3}} = (-J_4)S^2 + E_0,$$
$$E_{\mathrm{AFM4}} = J_4 S^2 + E_0.$$

Based on DFT total energy calculations, the superexchange interaction parameters at different pressures are summarized in Table 1. It can be seen that the superexchange interactions J_1 (via Fe–O–Fe) and J_3 (via Fe–O–P–O–Fe) play the dominant role in establishing the AFM ground state of α-LFP, while these exchange interactions are further strengthened with increasing pressure. A similar situation occurs in β-LFP, although the exchange interactions are weaker than in α-LFP.

To further explore the stability of the AFM ground states of α-LFP and β-LFP, the corresponding Néel temperatures (TN) are calculated using Monte Carlo simulations based on the classical Heisenberg model and the above calculated exchange interaction parameters. The TN of α-LFP is 47.5 K (see Fig. 4(a)), in good agreement with previous works.[38–41] Significantly, the TN increases to 70 K as pressure is increased to 16 GPa. Compared to α-LFP, β-LFP exhibits a lower TN (see Fig. 4(b)), indicating that α-LFP has a stronger ability to stabilize the AFM ground state against thermal fluctuations.

Table 1. Calculated exchange interaction parameters for LFP under pressure.

P (GPa)	J	J_1	J_2	J_3	J_4
α-LFP	0	−0.62	−0.05	−0.256	−0.01
	2	−0.68	−0.06	−0.27	−0.01
	4	−0.73	−0.06	−0.29	−0.02
	6	−0.77	−0.06	−0.30	−0.02
	8	−0.82	−0.06	−0.32	−0.03
	10	−0.88	−0.07	−0.34	−0.03
	12	−0.92	−0.07	−0.35	−0.03
	14	−0.97	−0.07	−0.36	−0.04
	16	−1.02	−0.07	−0.38	−0.04
	18	−1.07	−0.08	−0.39	−0.05
β-LFP	20	−0.06	−0.35	0.01	−0.19
	22	−0.07	−0.39	0.01	−0.2
	24	−0.08	−0.39	0.01	−0.21
	26	−0.06	−0.36	−0.01	−0.22
	28	−0.05	−0.42	0	−0.23
	30	−0.09	−0.43	0	−0.23

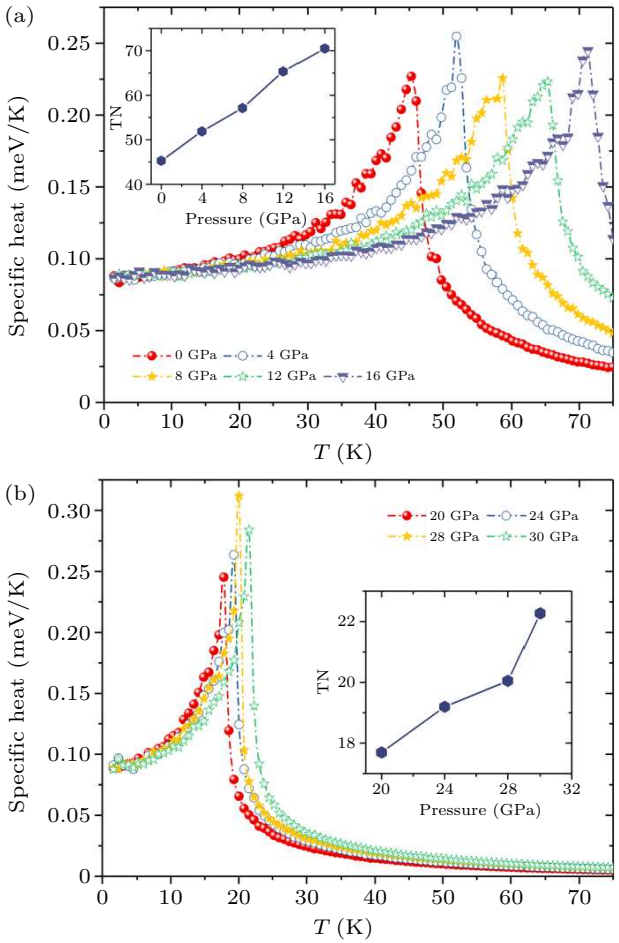


Fig. 4. (a) and (b) The specific heat of α-LFP and β-LFP as a function of temperature T under pressure, respectively. The inset shows the corresponding Néel temperature (TN) as a function of temperature T.

The exploration of Li^+ intercalation and deintercalation processes in LFP is crucial for its application as a cathode material in lithium-ion batteries. Therefore, we further investigate the phase transition pressure, bandgap, Li^+ migration barriers, and open-circuit voltage (OCV) of LFP as Li^+ is deintercalated. DFT calculations reveal that the volume decreases by 4.9%, with the lattice constant increasing along the b-axis and decreasing along the a-axis and c-axis, when α-LFP is completely delithiated to $FePO_4$ (see Fig. 5(a)). In contrast, β-LFP undergoes a larger structural deformation (8.2%) due to the corner-sharing structure among the three polyhedra. Notably, as the Li^+ concentration decreases, the critical pressure for the structural phase transition declines from 20 GPa to 6.95 GPa. Meanwhile, the band gap of α-LFP narrows as Li^+ is deintercalated, reaching a minimum value of 0.61 eV at $Li_{0.25}FePO_4$, and subsequently increases to 1.47 eV at $FePO_4$ (see Figs. 5(b) and S14). NEB calculations reveal that the Li^+ migration barrier decreases as Li^+ is deintercalated. In contrast, β-LFP exhibits a different phenomenon: it undergoes a transition from semiconductor to metal as Li^+ is deintercalated (see Figs. 5(b) and S15), while the Li^+ migration barriers are further increased (see Fig. 5(c)). To further elucidate the

potential performance of α-LFP and β-LFP, we calculate the corresponding OCV, which is closely related to the battery's energy density and power output. The OCV is defined by[42]

$$V = \frac{E_{\mathrm{Li}_{1-x_1}\mathrm{FePO_4}} - E_{\mathrm{Li}_{1-x_2}\mathrm{FePO_4}} + (x_1 - x_2)E_{\mathrm{Li}}}{x_1 - x_2}, \qquad (2)$$

where $E_{\mathrm{Li}_{1-x_1}\mathrm{FePO_4}}$ and $E_{\mathrm{Li}_{1-x_2}\mathrm{FePO_4}}$ are the total energies of $\mathrm{Li}_{1-x_1}\mathrm{FePO_4}$ and $\mathrm{Li}_{1-x_2}\mathrm{FePO_4}$, respectively, and E_{Li} is the total energy of an isolated Li atom. As shown in Fig. 5(d), the OCV of β-LFP is lower than that of α-LFP.

Compared to α-LFP, β-LFP has higher electronic conductivity, stronger mechanical properties, and comparable energy density. Therefore, a composite cathode material composed of α-LFP and a moderate fraction of β-LFP could serve as a promising candidate for next-generation cathode materials. Meanwhile, as demonstrated by AIMD simulations, a localized β-LFP phase can form within α-LFP under pressure. Thus, pressure may provide an effective strategy to modify $\mathrm{LiFePO_4}$, warranting further experimental exploration.

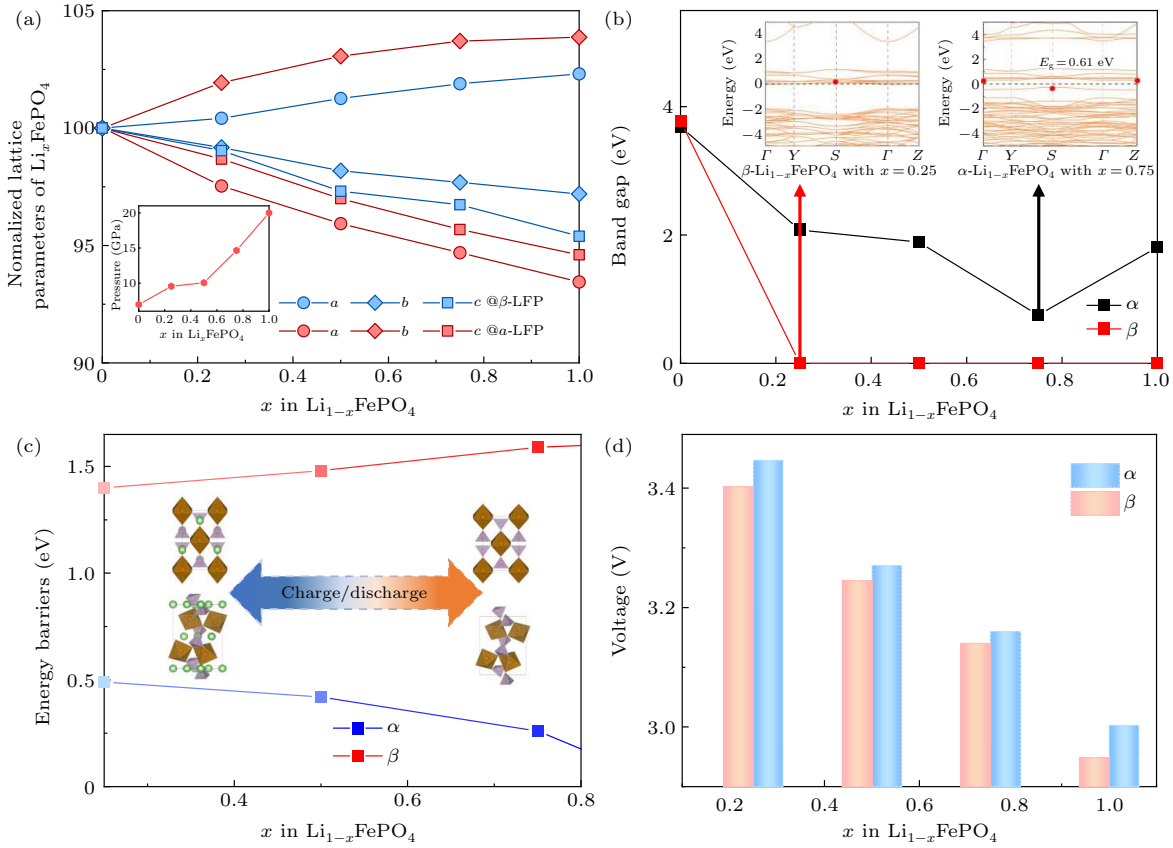


Fig. 5. (a)–(d) Lattice parameters, phase transition pressure, band gap, Li^+ migration barrier, and OCV of $\mathrm{Li}_{1-x}\mathrm{FePO_4}$ as a function of Li^+ concentration, respectively.

4. Conclusion

In summary, based on first-principles calculations, we systematically investigated the structural, electronic, and magnetic properties of α-LFP and β-LFP, and revealed that β-LFP has higher bulk, shear, and Young's moduli than α-LFP. Since Li–O–Fe bonds are weaker than Li–O–Li bonds, LFP is particularly sensitive to pressure along the [001] direction. The results of AIMD simulations indicate that the anisotropic compression of Li–O bonds under pressure is the primary factor driving the structural phase transition. Regarding ion transport, the Li^+ migration barrier of β-LFP is higher than that of α-LFP and further increases with increasing pressure. It is worth noting that negative nearest- and next-nearest-neighbor exchange interactions enable α-LFP and β-LFP to maintain AFM ground states, and the corresponding Néel temperatures can be further enhanced by increasing pressure. In addition, β-LFP undergoes a transition from semiconductor to metal due to the presence of Fe^{3+} induced by delithiation. This work enriches the physical property data for $\mathrm{LiFePO_4}$ and is relevant for optimizing its electrochemical performance under special operating conditions such as high pressure.

Acknowledgments

Project supported by the National Natural Science Foundation of China (Grant No. 12304089) and the start-up foundation from Shanghai University. Calculations were partially performed on computers at the Shanghai Technical Service Center for Scientific and Engineering Computing, Shanghai University.

References

[1] Albertus P, Anandan V, Ban C, *et al.* 2021 *ACS Energy Lett.* **6** 1399
[2] Tao R, Gu Y, Du Z, Lyu X and Li J 2025 *Nat. Rev. Clean Technol.* **1** 116
[3] Li L, Wu L, Wu F, Song S, Zhang X, Fu C, Yuan D and Xiang Y 2017 *J. Electrochem. Soc.* **164** A2138
[4] He J, Meng J and Huang Y 2023 *J. Power Sources* **570** 232965
[5] Padhi A K, Nanjundaswamy K S and Goodenough J B 1997 *J. Electrochem. Soc.* **144** 1188
[6] Yamada A, Chung S C and Hinokuma K 2001 *J. Electrochem. Soc.* **148** A224
[7] Liu H, Strobridge F C, Borkiewicz O J, Wiaderek K M, Chapman K W, Chupas P J and Grey C P 2014 *Science* **344** 1252817
[8] Wang W, Wang R, Zhan R, Du J, Chen Z, Feng R, Tan Y, Hu Y, Ou Y, Yuan Y, Li C, Xiao Y and Sun Y 2023 *Nano Lett.* **23** 7485
[9] Zhao X, Wang X, Guo J, Gu Z, Cao J, Yang J, Lu F, Zhang J and Wu X 2024 *Adv. Mater.* **36** 2308927
[10] Cao M, Liu Z, Zhang X, Yang L, Xu S, Weng S, Zhang S, Li X, Li Y, Liu T, Gao Y, Wang X, Wang Z and Chen L 2023 *Adv. Funct. Mater.* **33** 2210032
[11] Chung S, Bloking J and Chiang Y 2002 *Nat. Mater.* **1** 123
[12] Ouyang C, Wang D, Shi S, Wang Z, Li H, Huang X and Chen L 2006 *Chin. Phys. Lett.* **23** 61
[13] Shi S, Liu L, Ouyang C, Wang D, Wang Z, Chen L and Huang X 2003 *Phys. Rev. B* **68** 195108
[14] Li H, Wang Z, Chen L and Huang X 2009 *Adv. Mater.* **21** 4593
[15] Li Z, Zhang D and Yang F 2009 *J. Mater. Sci.* **44** 2435
[16] Andersson A S and Thomas J O 2001 *J. Power Sources* **97** 498
[17] Gai J, Yang J, Yang W, Li Q, Wu X and Li H 2023 *Chin. Phys. Lett.* **40** 086101
[18] Li Y, Sun S, He Y and Li H 2022 *Chin. Phys. Lett.* **39** 026101
[19] Du J, Tao H, Chen Y, Yuan X, Lian C and Liu H 2021 *Chin. Phys. Lett.* **38** 118201
[20] Axmann P, Stinner C, Wohlfahrt-Mehrens M, Mauger A, Gendron F and Julien C 2009 *Chem. Mater.* **21** 1636
[21] García-Moreno O, Alvarez-Vega M, García-Alvarado F, García-Jaca J, Gallardo-Amores J, Sanjuán M and Amador U 2001 *Chem. Mater.* **13** 1570
[22] Lin H and Zeng Z 2011 *IEEE Trans. Magn.* **47** 3817
[23] Dong H, Guo H, He Y, Gao J, Han W, Lu X, Yan S, Yang K, Li H, Chen D and Li H 2017 *Solid State Ion.* **301** 133
[24] Wu C, Huang W, Liu L, Wang H, Zeng Y, Xie J, Jin C and Zhang Z 2016 *CrystEngComm* **18** 7707
[25] Guo H, Song X, Zhuo Z, Hu J, Liu T, Duan Y, Zheng J, Chen Z, Yang W, Amine K and Pan F 2016 *Nano Lett.* **16** 601
[26] Hohenberg P and Kohn W 1964 *Phys. Rev.* **136** B864
[27] Kresse G and Furthmüler J 1996 *Phys. Rev. B* **54** 11169
[28] Liechtenstein A I, Anisimov V I and Zaanen J 1995 *Phys. Rev. B* **52** R5467
[29] Henkelman G, Uberuaga B P and Jónsson H 2000 *J. Chem. Phys.* **113** 9901
[30] Parrinello M and Rahman A 1980 *Phys. Rev. Lett.* **45** 1196
[31] Ouyang C, Shi S, Wang Z, Huang X and Chen L 2004 *Phys. Rev. B* **69** 104303
[32] Pei B, Yao H, Zhang W and Yang Z 2012 *J. Power Sources* **220** 317
[33] Maxisch T and Ceder G 2006 *Phys. Rev. B* **73** 174112
[34] Zhang Z, Ma H and Wan B 2024 *JOM* **77** 2943
[35] Zeng G, Caputo R, Carriazo D, Luo L and Niederberger M 2013 *Chem. Mater.* **25** 3399
[36] Fisher C A J, Hart Prieto V M and Islam M S 2008 *Chem. Mater.* **20** 5907
[37] Adams S and Prasada Rao R 2011 *Solid State Ion.* **184** 57
[38] Santoro R and Newnham R 1967 *Acta Cryst.* **22** 344
[39] Li J, Garlea V, Zarestky J and Vaknin D 2006 *Phys. Rev. B* **73** 0234410
[40] Werner J, Neef C, Koo C, Zvyagin S, Ponomaryov A and Klingeler R 2020 *Phys. Rev. Mater.* **4** 115403
[41] Shi S, Ouyang C, Xiong Z, Liu L, Wang Z, Li H, Wang D, Chen L and Huang X 2005 *Phys. Rev. B* **71** 144404
[42] Zhang Y, Alarco J, Best A, Snook G, Talbot P and Nerkar J 2019 *RSC Adv.* **9** 1134